Received: October 28, 2024. Revised: December 18, 2024.

International Journal of
Intelligent Engineering & Systems

http://www.inass.org/

Enhanced Brain Tumor Detection from Microwave Imaging with Hybrid Inception-CNN and UWB Circular Monopole Patch Antenna

Deebu U S[1]* **Sreeja T K[2]**

[1]*Department of Electronics and Communication Engineering,*
Noorul Islam Centre for Higher Education, Tamil Nadu, India
[2]*Department of Nanotechnology, Noorul Islam Centre for Higher Education, Tamil Nadu, India*
* Corresponding author's Email: Deebu.us.321@outlook.com

Abstract: Brain tumors are among the most prevalent tumor types worldwide. When tissues grow abnormally, they form a tumor. It is classified according to its anatomical location and dimensions. Positron Emission Tomography (PET) scans, Magnetic Resonance Imaging (MRI), biopsies, Computerized Tomography (CT) scans, lumbar punctures, myelograms, Electroencephalograms (EEG), and other methods are available for the diagnosis of brain tumors. The existing approaches are non-invasive but constrained by cost and reliability concerns. The diagnostic procedures are inadequate for detecting tumors beyond a depth of 20% and raise significant concerns about the consequences of ionizing radiation. The radiative effect of the microwave imaging system could serve as a beneficial way to find brain tumors early on because it makes up for the problems with current diagnostic methods for ionizing effects. The proposed work's main goal is to design an effective deep learning approach for identifying brain tumors from microwave brain images. The proposed approach mainly consists of two phases. During the initial phase, an Ultra-Wide Band (UWB) circular monopole patch antenna has been designed for microwave imaging of brain tumors. The generated microwave brain images are fed into the proposed hybrid inception- CNN based brain tumor detection system in the second phase. These extracted features using the inception- CNN model is passed through the fully connected layer for efficient brain tumor classification. The simulation results indicates that the proposed brain tumor detection model using microwave brain images attained better detection performance, with an accuracy of 99.48 %. It also emphasizes how effectively medical imaging techniques can improve detection performance by incorporating artificial intelligence.

Keywords: Brain tumors, Microwave imaging, Ultra-wide band antenna, Patch antenna, Artificial intelligence, Deep learning, Convolutional neural network, Inception network.

1. Introduction

A brain tumor is an aggregation of abnormal brain cells. A primary brain tumor initiates within the brain, whereas a secondary or metastatic brain tumor arises from cancer that has disseminated to the brain from other regions of the body [1]. The brain tumour's increasing size and position demonstrates its impact on the functions of the nervous system. According to the type, location, and size of the brain tumor, advanced technological procedures are used for both diagnosis and therapy. Microwave Imaging (MI) is utilized to identify hidden objects within the human body using electromagnetic (EM) waves in the frequency range of 300 MHz to 300 GHz. MI is a technique where the EM wave interfaces with a suspected body part, and the performance parameters of the reflected wave, such as Specific Absorption Rate (SAR), Return Loss (RL), and current density, are compared with the parameters. Environmental factors, including temperature, humidity, and other factors, can effectively impact the characteristics of reflected signals [2], so these factors should also be considered.

The MI method is introduced as a substitute to X-ray, MRI, CT scan, PET scan, and other modalities because of its non-invasive nature.

Received: October 28, 2024. Revised: December 18, 2024.

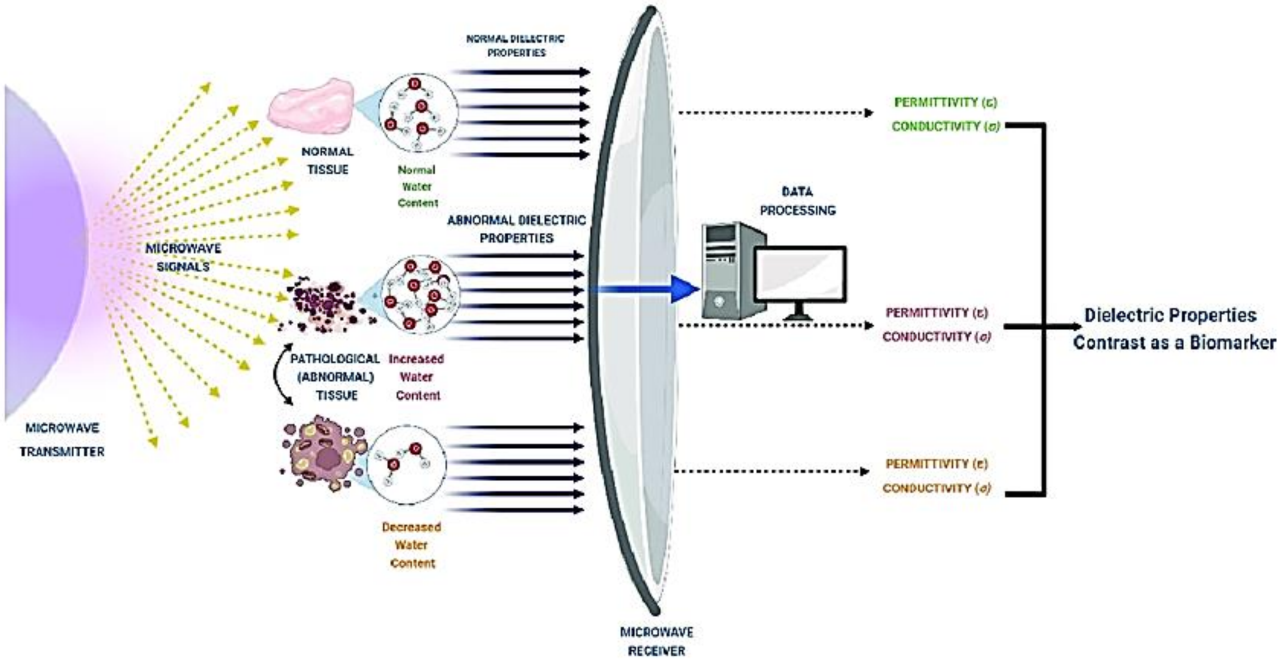

Figure. 1 Principle of sensing based on the contrast of dielectric characteristics utilizing microwaves [4]

The MI method uses the scattering principle, which said that waves are scattered or reflected because benign and malignant brain tumors have different dielectric properties. This approach identifies the differential water content levels in soft tissues with and without tumors. In this method, Ultra-Wide Band (UWB) antennas send short pulses of low-power microwave energy into the brain [3]. The brain uses the backscattered energy to figure out where the antenna is and turn the signal into a 3D image. The greater water content in the tissue's accounts for the dielectric characteristics of tumors compared to normal tissue.

The UWB antenna is a crucial component of the MI technique. The MI device frames the organ under study, such as the brain, with a single antenna or an array of antennas. One antenna function as a transmitter, while others serve as receiver antennas, facilitating the scattering of signals from the brain, including blood, tumors, and tissues. When electromagnetic waves interact with the human body, they alter the permittivity and conductivity of the brain's medium, providing the basis for MI-based tumor detection in the brain. Fig. 1 shows the general idea behind employing microwaves to detect the dielectric variation between healthy and abnormal tissues depending on water content.

Microstrip Patch Antennas (MPAs) have very simple geometric configurations [5, 6]. It comprises four components: (i) a radiating element or patch, (ii) a ground plane, (iii) a dielectric substrate, and (iv) a feeding network, displayed in Fig. 2.

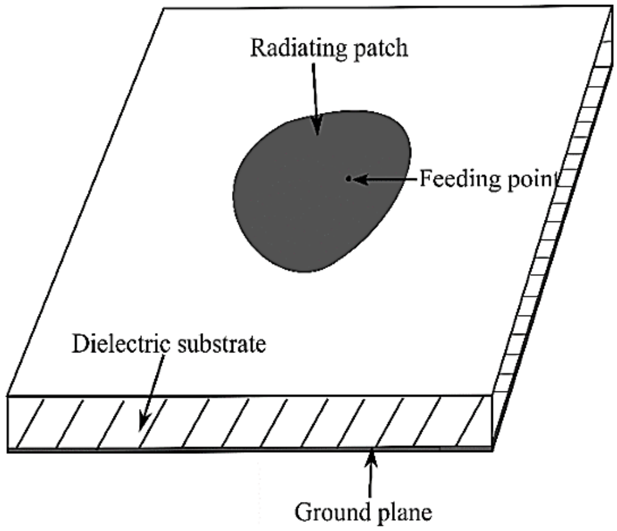

Figure. 2 General Configuration of MPA

The microstrip patch comprises of a conductive patch attached to a dielectric substrate, with the reverse side grounded. When current flows through a feed line to the antenna strip, it produces electromagnetic waves. The propagation of waves from the patch's edges forms a radiation pattern. If the substrate is too thin, the waves reflect off its edges. Patch antennas are inefficient because they only radiate a part of energy. It functions more as a cavity than as a transmitter.

Artificial Intelligence (AI) holds significant potential for enhancing the reliability and accuracy of brain tumor detection. AI systems are more accurate than traditional approaches at analysing complex medical images [7]. This leads to more accurate tumor type identification and earlier detection, which is effective for timely and effective treatment. Therefore, AI has the potential to transform brain tumor diagnostics and enhances patient outcomes. This paper proposes an effective brain tumor detection system using AI from microwave brain images incorporated with UWB circular monopole patch antenna. The major objectives of the proposed methodology include:

- Development of UWB circular monopole patch antenna for microwave imaging.
- Generation of new microwave brain image dataset for brain tumor detection.
- Implementation of brain tumor detection framework employing hybrid Inception-CNN model from microwave images.

The suggested strategy primarily consists of two stages. An ultra-wideband (UWB) circular monopole patch antenna was created in the first phase for the purpose of imaging brain tumors using microwaves. In the second phase, the generated microwave brain images are fed into the suggested hybrid inception-CNN-based system for detecting brain tumors. For effective brain tumor classification, these features, which were extracted using the Inception-CNN model, are sent through the fully connected layer.

The remaining portions of the paper are structured as follows: Section 2 offers an overview of the existing research, emphasizing areas necessitating further exploration. Section three offers a comprehensive explanation of the methodology. Section 4 presents the findings derived from the proposed methodology in detail. The study concludes by summarizing and evaluating the results in Section 5.

2. Literature review

Niloy Goswami and Md. Abdur Rahman [8] designed patch antennas, which are particularly useful for employing the monostatic technique to identify brain tumors inside a human head phantom. These antennas are simple to fabricate and function effectively across a broad frequency range. The study examined all relevant factors for the four stages of the proposed antenna's modelling, which used FR 4 as the substrate material. The investigation used a human head phantom framework to evaluate important performance metrics. The most notable finding indicated that the antenna was capable of accurately detecting tumors because it showed a significant difference in S_11 and SAR when tumors are present. The major limitation of the proposed study is that the variation in tissue composition, density and electrical property, which could affect the accuracy of tumor detection. Md. Samsuzzaman et al. [9] used a defected grounded low SAR monopole patch antenna to make a circular slotted patch that could be used for biomedical imaging and micro-wave-based object identification. Prototype antennas were constructed and experimentally validated to evaluate design accuracy on FR 4 substrates. The fidelity factors of the antenna were calculated for three potential configurations. A 9-antenna array positioned around a 3-D; realistic Hugo-head structure was subjected to behaviour analysis using the 3D electromagnetic CST simulator. The analysis produced acceptable findings and demonstrated the usefulness of the suggested antenna in the designed MI application. But the major drawback is that the substrate has relatively high loss at microwave frequencies. Musa N. Hamza et al. [10] proposed an enhanced sensor and microstrip antenna architecture for non- invasive brain cancer and breast cancer diagnostics. The antenna's design incorporated a hybrid configuration of microstrip patches and a Vivaldi-like structure. The base antenna, located 3 mm from the main radiator on a different substrate, connects to the Artificial Magnetic Conductor (AMC) unit to implement the sensor. According to the simulation results, tumors of different sizes, including those as small as 0.5 mm, can be identified by the MI system using the suggested sensor. But the performance of the system is limited for detecting tumors located deeper within tissues. H. Vinod Kumar and T.S. Nagaveni [11] developed a MPA for breast cancer detection. The patch antenna's rectangular form placed it 1.5 cm away from the phantom. The acquired experimental data demonstrated the efficiency of the suggested design, closely matching both the simulated outcomes and the theoretical models. But due to the placement of antenna, it cannot replicate the exact conditions of in-vivo tissue conditions.

Ahasan Kabir and Ishrat Jahan [12] developed two different kinds of 3D breast phantoms and a MPA that operated in the Industrial Scientific Medical (ISM) frequency spectrum. The goal of this research was to employ SAR analysis and variance analysis of S_11 parameters to identify malignant tumors within a breast phantom. The simulation results demonstrated that the antenna can detect cancerous tumors in a simulated breast phantom. The applicability in clinical diagnostics can be limited due to strict safety standards and regulations related to energy depositions in human tissue. Rakesh Singh et al. [13] developed a small antenna that could work with a breast phantom and in the frequency range of 1 to 6 GHz, in order to find the dielectric contrast between healthy and cancerous tissue. This study illustrated the importance of considering the permittivity of phantom when designing the sensor. The simulation results indicated that the suggested sensor and the breast phantom are compatible, emphasizing the sensor's potential importance for microwave imaging system. The study only discussed about the dielectric contrast. Devendra Kumar and Dhirendar Mathur [14] developed an inexpensive and discrete antenna operating in the ISM band. It has been clearly shown that using a soft surface can effectively reduce back radiation. The inherent properties of the flexible Ethylene Vinyl Acetate (EVA) foam substrate encompassed waterproofing, UV resistance, and mechanical stability. The physical characteristics of the substrate material, along with its low SAR and broadside radiation pattern oriented away from the body, make it a viable option for data communications in the healthcare industry. The limited frequency band restricted its applicability in situations requiring multiband or wide band operation. Sadiq Alhuwaidi and Tanghid Rashid [15] developed and fabricated a wearable pentagon MPA in the ISM band. The first phase involved a simulation of the redesigned pentagon MPA. The second step involved using simulations of microwave computer-aided design software to create comprehensive field theory solutions. Finally, the third stage focused on the fabrication of the proposed antenna. At this stage, simulations were conducted to evaluate the spectrum of electromagnetic wave absorption by a human head model by calculating the SAR at different locations. Various environmental factors affect the antenna performance.

Abdul Wajid et al. [16] offered a performance comparison between an electromagnetic bandgap (EBG)-based dual-band design and a split-ring resonator (SRR)-based dual-band antenna functioning at 2.4 GHz and 5.4 GHz. A dielectric material used in garments was combined with metamaterial surfaces to provide protection against electromagnetic radiation hazards. A bending test was performed to measure the performance of three suggested antennas. The outcomes showed that the design exhibited exceptional flexibility and resilience against bending without compromising antenna performance. The major drawback of the proposed antenna design are limited frequency range and specific material dependency. Pillalamarri Laxman and Anuj Jain [17] proposed an antenna configuration of four fundamental components arrayed orthogonally in opposition to one another. The proposed antenna functions securely even close to the human body, with no negative radiation-related health impacts. The orthogonal composition of antenna could complicate the proposed design. Mohammed E. Yassin et al. [18] designed a strip antenna, which is G- shaped, fabricated on a flexible substrate for off-body biomedical communication. The antenna's design achieved circular polarization within frequency range of 5 to 6 GHz, enabling communication with WiMAX/WLAN antennas. The design features created a distinctive 'G' or inverted 'G' configuration. The design parts are made up of a semicircular strip that is horizontally extending at the bottom, connected at the top by a corner-shaped strip extension, and topped with a small circular patch. According to the simulation findings, the antenna reached a 3 dB axial ratio (AR) Bandwidth (BW) of 18% in the 5 to 6 GHz frequency range. The study is limited to antenna size and design complexity. Mohammed Saif ur Rahman et al. [19] proposed microwave non-destructive testing (NDT) for composite structures incorporated with antennas. A high-resolution image of a C-band patch antenna mounted on an aramid paper-based honeycomb substrate shielded in a GFRP sheet was produced using a low-frequency planar resonator probe. The study focused on NDT's MI capabilities and benefits when looked at structures. It compared the results to those of a K-band rectangular aperture probe to show how useful it could be for smart structure inspection. The study limited to its applicability in complex structures.

In medical and microwave NDT, patch antenna designs have several drawbacks. Their inadequate resolution and susceptibility to dielectric fluctuations limit an analysis of the interior structure of composite materials beyond a certain depth. Because of interference from the antennas themselves, detecting defects and evaluating the material state of structures with embedded antennas may become more challenging. Despite having a large BW, these antennas could not offer the breadth required for some medical applications. Their functionality is very dependent on the surroundings when it comes to being on or near the human body. These elements can cause signal attenuation and distortion, and they include proximity to clothing, other objects, and body tissues. Furthermore, variations in object emissivity based on material, surface finish, and circumstances pose challenges to accurate antenna design and simulation. Miniature antennas usually compromise efficiency and BW, making them unsuitable for covering a large frequency range.

3. Materials and methods

The suggested approach comprises two different phases. During the initial phase, the microwave brain images are acquired with the help of the designed UWB circular monopole patch antenna. The generated microwave brain images are fed to the proposed hybrid Inception- CNN framework for brain tumor detection. The thorough framework of the suggested brain tumor detection model is described below.

3.1 Design of ultra-wide band (UWB) circular monopole patch antenna for microwave brain imaging

The slotted UWB circular monopole patch antenna is specifically designed for microwave brain imaging applications. This antenna incorporates an inverted U-shaped Defected Ground Structure (DGS) into its construction on the ground plane. The antenna's design allows for resonance at both 7.68GHz and 4.6GHz, resulting in a directivity of 6.69 dB and a gain of 5.52 dB. At the higher frequency of 7.68 GHz, the antenna displays a RL of -48.3 dB, suggesting effective impedance matching is appropriate for high-resolution imaging. The simulated antenna design's construction and evaluation validate its functional effectiveness across a wide range of frequencies. The antenna is designed to achieve compact size. The design of the UWB circular patch antenna aims to improve directivity.

UWB circular patch antennas are designed and optimized with the aid of ANSOFT HFSS. The suggested antenna has dimensions of 65 x 50 x 1.6 mm^3.The evaluation is performed on a FR4 substrate considered by a dielectric constant of 4.4, a loss tangent of 0.025, and a thickness of 1.6 mm. This antenna was created using mathematical modelling techniques. Eq. (1) is employed to compute the antenna's resonance frequency.

$$F_r = \frac{1.841\nu_0}{2\pi r\sqrt{\delta}} \tag{1}$$

Where the speed of light in free space is represented by ν_0.

Eq. (2) is employed to compute the radius of the circular patch.

$$a = \frac{F}{\sqrt{\left[1+\frac{2h}{\epsilon_r \pi F}\left[\ln\left(\frac{\pi F}{2h}\right)+1.7726\right]\right]}} \tag{2}$$

The directivity of the circular patch antenna in terms of function parameter γ is given as in Eq. (3).

$$D(\gamma) = 4.77142 - 0.12087\gamma + 2.9853\gamma_2 - 1.25954\gamma_3 + 1.25337\gamma_4 - 0.50481\gamma_5\, dB \tag{3}$$

The physical dimensions of the fabricated antenna are tabulated in Table 1. The substrate, serving as the antenna's basis, measures 50 mm in length and 65 mm in width. The circular patch, which has an 11 mm radius and is a critical component of the design, affects the antenna's radiation characteristics.

The defected ground plane, a critical component for enhancing BW and impedance matching, measures 24.5 mm in length. The feed line, which is responsible for signal transmission to the antenna, measures 37 mm in length and has a width that varies by 1.6 mm. The structure of top part of proposed circular antenna and structure of bottom part of proposed circular antenna is shown in Fig. 3 and Fig. 4 respectively.

The radio frequency Surface Mount Adapter (SMA) is utilized to excite the slotted circular monopole patch antenna, which was successfully constructed according to the simulated design. This procedure required connecting the SMA adapter to the antenna to enable signal transmission. In order to guarantee stability and appropriate grounding, the upper and lower pins of the five-pin connector were carefully placed on the ground plane. The central pin of the connector was carefully imprinted onto the conductive strips of the antenna, ensuring a strong and effective connection. The performance of the antenna was maximized, and dependable signal propagation was ensured. The top part and bottom part of fabricated antenna is visualized in Fig. 5 and Fig. 6 respectively. Fig. 7 illustrates the 9- antenna array system.

Table 1. Physical Dimension of Proposed Antenna

Parameter	Label	Design Value (mm)
Substrate Length	L	50
Width of substrate	W	65
Circle Radius	R	11
Length of defected ground plane	L_g	24.5
Length of Feed Line	L_f	37
Width of Feed Line	W_f	1.6

Received: October 28, 2024. Revised: December 18, 2024.

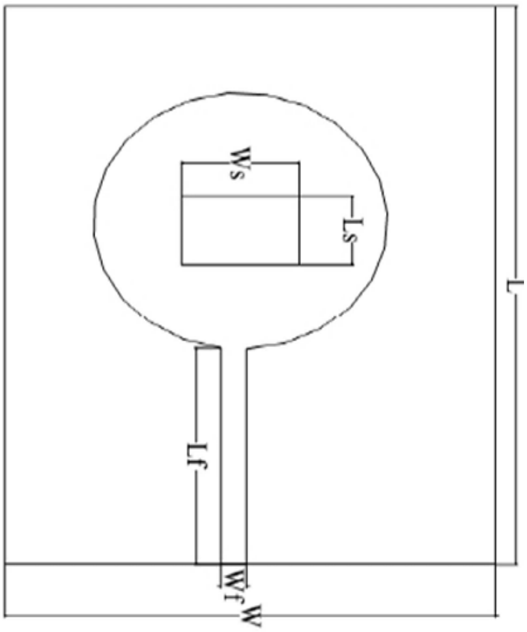

Figure. 3 Structure of Top Part of Proposed Circular Antenna

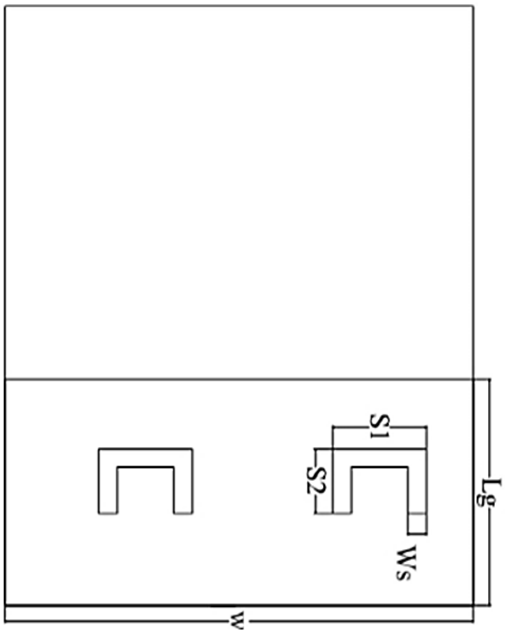

Figure. 4 Structure of Bottom Part of Proposed Circular Antenna

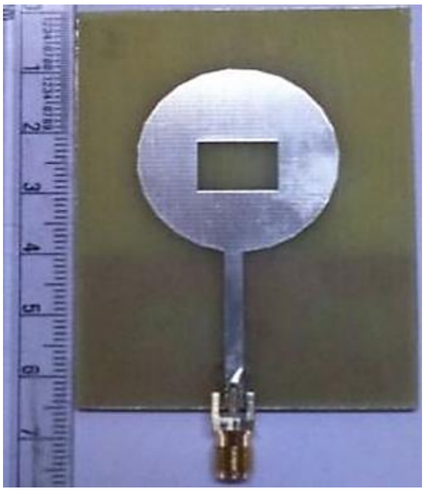

Figure. 5 Top Part of Fabricated Antenna

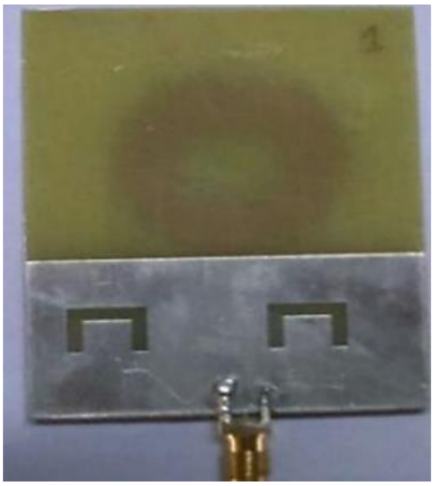

Figure. 6 Bottom Part of Fabricated Antenna

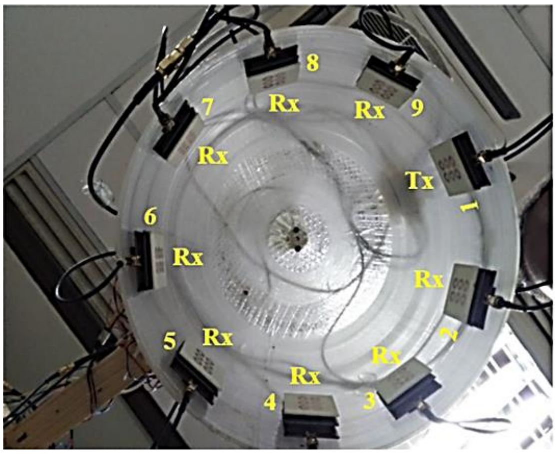

Figure. 7 9- antenna array System

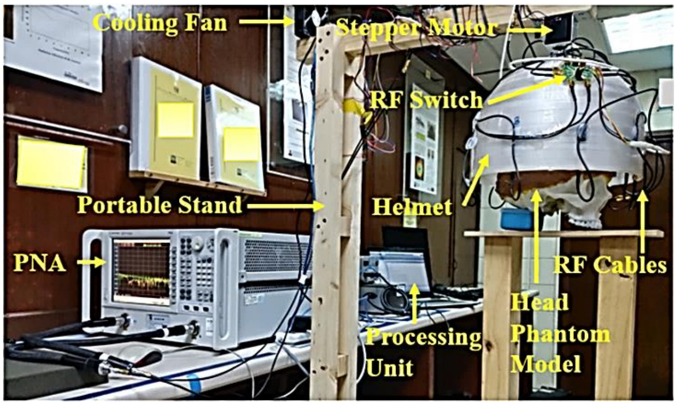

Figure. 8 Overall Imaging Framework

 DOI: 10.22266/ijies2025.0229.88

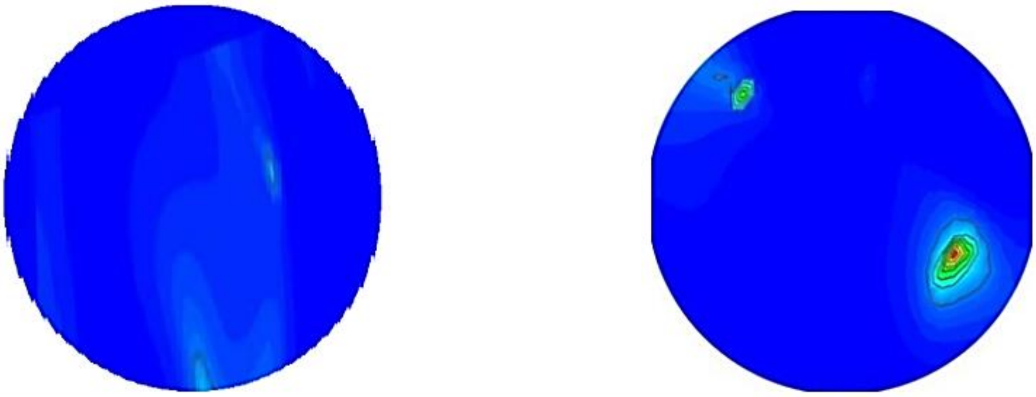
(a) (b)
Figure. 9 Microwave Brain Images: (a)Healthy and (b)Tumor

The suggested system consisted of PNA E8358A transceivers, a microprocessor, a stepper motor, a portable platform, an RF switch, nine antenna arrays, and a specially designed half-elliptical helmet. The overall imaging framework is shown in Fig. 8.

The portable platform fixes the stepper motor, enabling it to cover the entire 360° surface by rotating clockwise at an angle of 7.2° with each step. The motor shaft connects the motor and the helmet. The helmet has a diameter of 250 mm. As the transmitting antenna rotates, the receiving antenna collects signals that enter the brain. The signals are reconstructed to provide microwave brain images. Fig. 9 displays the microwave brain images generated with the fabricated patch antenna.

3.2 Brain tumor detection from microwave brain images using hybrid inception-cnn model and hyper parameter tuning

The suggested brain tumor detection model uses CNN as its base model. The Inception network captures multi-scale features by employing convolution with varying kernel sizes. Batch normalization, regularization, and dropout optimize the model. Fig. 10 illustrates the comprehensive block diagram of the suggested brain tumor detection framework.

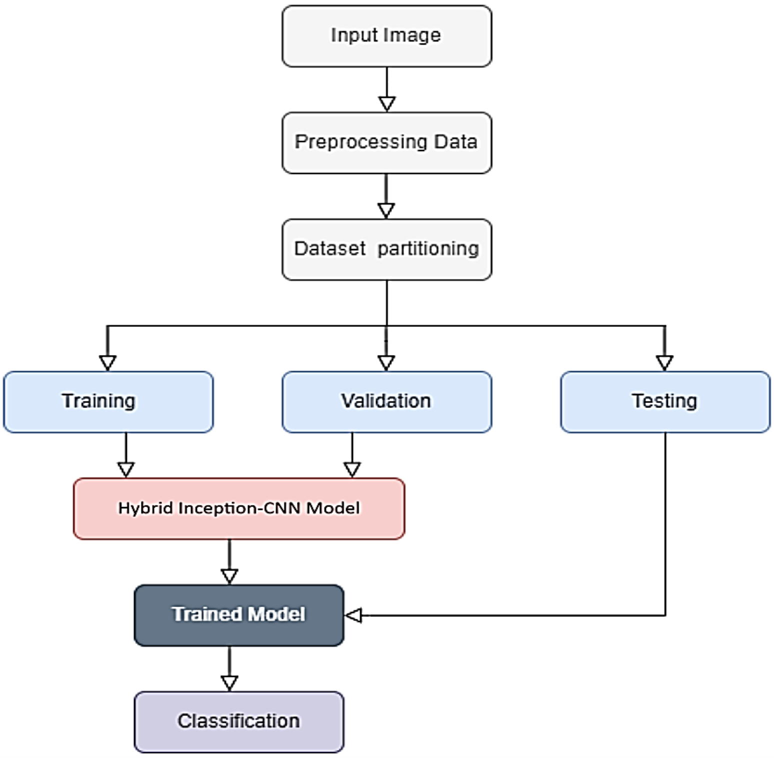

Figure. 10 Block Diagram of Suggested Brain Tumor Detection System

Received: October 28, 2024. Revised: December 18, 2024.

3.2.1. Dataset description

The images are acquired using patch antennas from the proposed imaging system. It is essential to implement a non-invasive and simple diagnostic method to minimize costs. A new dataset is generated utilizing microwave brain imaging for tumor detection. This dataset comprises two categories: tumor and healthy, displayed in Fig. 11. All image classes are in.png format. The images are 256 ×256 in size.

The dataset contains 1,282 images, with 672 classified as tumors and 610 as normal. A total of 1,026 images are preferred for training, while the remaining 256 images are allocated for testing. This proportional splitting provides an extensive training set while preserving an adequate quantity of images for testing and assessing the model. Fig. 12 depicts the distribution of classes within the dataset.

3.2.2. Data preprocessing and data splitting

Data preprocessing techniques can enhance the quality and applicability of image data. This study used a range of data preprocessing techniques, including cropping, image augmentation, and image normalization. Cropping an image involves removing unnecessary background elements to emphasize the central region. Fig. 13 illustrates the microwave brain images before and after cropping.

Normalization improves the model’s convergence and performance by standardizing pixel values to a uniform range. Image augmentation techniques such as rotation, flipping, shear transformations, brightness adjustments, and width and height shifts increase the dataset’s diversity. Lastly, the data is divided into a 75:15:10 ratio, in which training uses 75 percent of the data, validation uses 15 percent, and testing uses 10 percent.

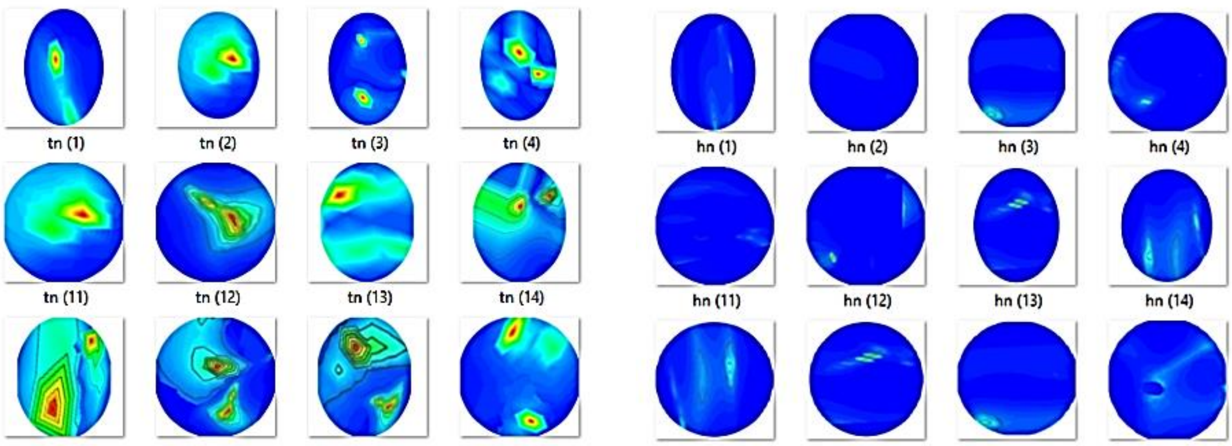

(a) (b)

Figure. 11 Sample Microwave Brain Images from dataset: (a)Tumor and (b)Healthy

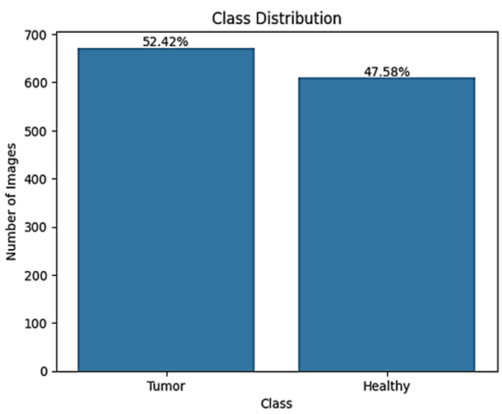

Figure. 12 Class Distribution

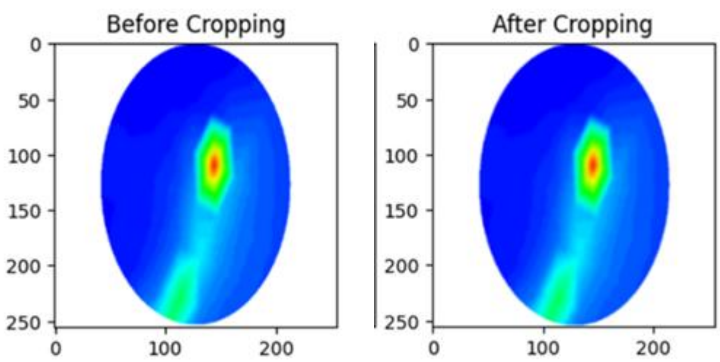

(a) (b)

Figure. 13 Microwave Brain Images: (a)Before Cropping and (b)After Cropping

 DOI: 10.22266/ijies2025.0229.88

3.2.3. Proposed hybrid inception- CNN model for brain tumor detection

The input layer of this CNN model processes images with dimensions of 256 × 256 × 3 for image classification. It consists of many convolutional blocks, each incorporating convolutional layers with Rectified Linear Unit (ReLU) activation, batch normalization, max pooling, and dropout layers to mitigate overfitting. The model has inception modules that combine several convolutional pathways to gather a wide range of spatial data, which makes it better at detecting complex patterns. The model employs regularization strategies like L2 regularization and higher dropout rates to improve generalization and reduce the likelihood of overfitting. The network ends with a Fully Connected (FC) layer that outputs the final classification by sigmoid activation.

The primary objective of CNN is feature extraction, followed by feature fusion and classification [20]. CNN generates feature classifications based on sample data that it collects, as well as distinguishing properties. The CNN approach employs a series of processing layers, each of which advances from low to high complexity by learning new representational abilities. By offering information that may subsequently be utilized to find higher-level features, these characteristics allow the CNN to operate as an independent feature extractor. The convolutional layer, activation function layer, pooling layer, and FC layer are the four main types of layers in the basic CNN framework, illustrated in Fig. 14.

The convolutional layer is an essential element of the CNN architecture. This layer calculates the dot product between two matrices: the set of learnable parameters, often known as a kernel, and a limited subset of the provided image pixels. The kernel is spatially lesser than the image, but it has more depth. This signifies that the kernel's height and width will be limited, whereas the depth will include all 3 RGB channels [21]. A convolution operation that applies a kernel to input images directs forward propagation in CNN, as shown by Eq. (4).

$$(I * K)\,[i,j] = \sum_{p=0}^{m-1} \sum_{q=0}^{n-1} I[i-p, j-q]\,K\,[p,q] \quad (4)$$

Here, I represent the input, while K is the filter with dimensions m × n.

The convolution process is illustrated in Fig. 15. After obtaining the feature maps, pooling (sub-sampling) layer and a convolution layer added to the CNN. The pooling layer must reduce the convolved feature's spatial size. A reduction in dimensionality results in a decrease in the computational power required for data processing. This preserves the model's practical training and facilitates the extraction of positional and rotational invariant leading features.

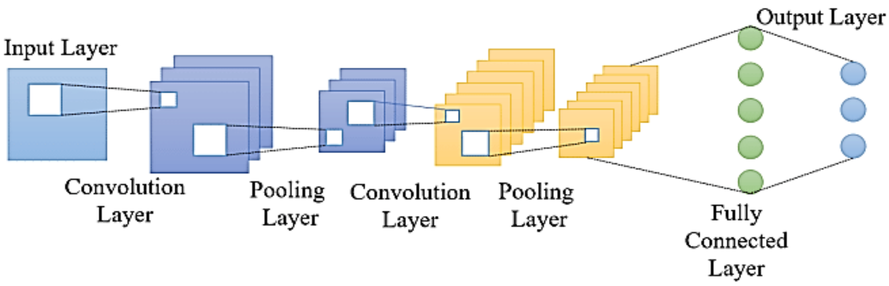

Figure. 14 Basic CNN Architecture

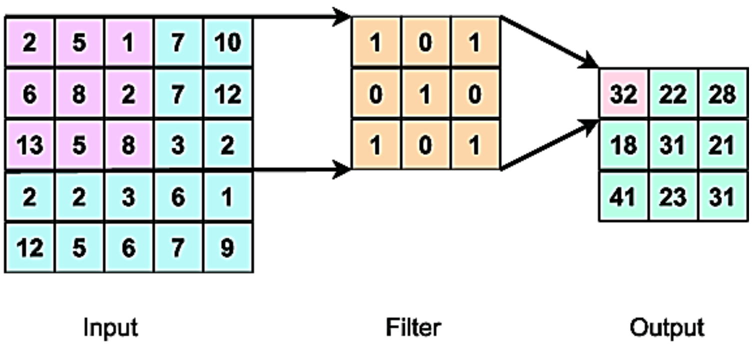

Figure. 15 Visualization of Convolution Operation

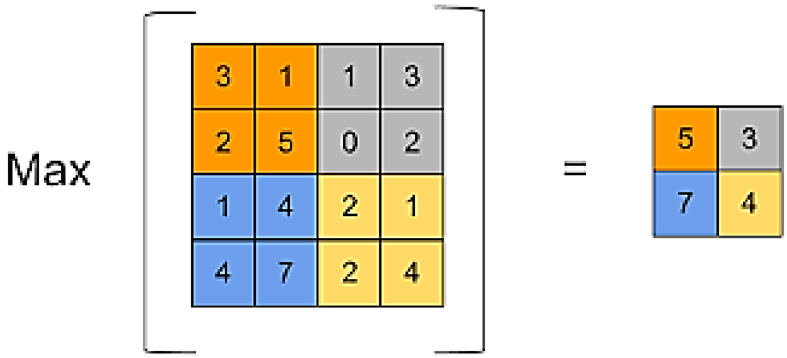

Figure. 16 Visualization of Max-pooling Operation

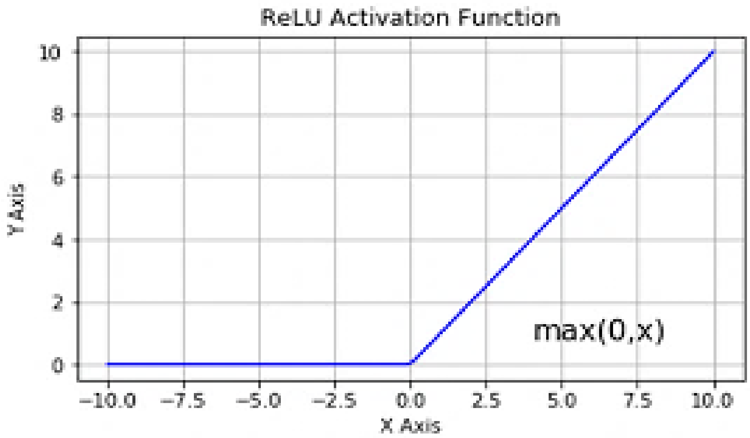

Figure. 17 Visualization of ReLU Activation Function

Pooling minimizes overfitting and reduces training time. Max pooling refers to the pooling method that chooses the maximum value from the area of the feature map enclosed by the filter [22]. Thus, the feature map generated by the max-pooling layer includes the most salient characteristics from the preceding feature map. The max- pooling process is visualized in Fig. 16.

The activation function is crucial in CNN layers. The activation function, a distinct mathematical function, receives the filter's output. ReLU is the most often utilized activation function in CNN feature extraction [23]. The main goal of using the activation function is to determine the NN's output, specifically whether it is yes or no. The activation function changes the output values from 0 to 1, or from 1 to 1. The ReLU function can be mathematically represented as in Eq. (5). Fig. 17 represents the graphical representation of ReLU function.

$$f(x) = \max(0, x) \tag{5}$$

The inception module in the suggested system comprises a combination of various convolutional layers to capture spatial features. This module processes the input through multiple concurrent channels: a max pooling layer with a 3×3 filter, followed by a 1×1 convolution; a direct 1×1 convolution; and a 1×1 convolution to reduce dimensionality, followed by another 1×1, 3×3, or 5×5 convolution. Each of these steps utilizes L2 regularization and ReLU activation. The Inception module then concatenates the outputs from all pathways to form the final output, which it then passes on to the following layer. This multi-path technique lowers the computational cost while enabling the network to capture spatial data at various scales and enhance the model's detection performance of intricate patterns. Fig. 18 shows the block diagram for the inception block.

In the suggested model, batch normalization is employed after each convolutional layer to stabilize the learning process by normalizing the layer inputs. The normalization is performed by calculating the mean (μ) and variance (σ^2) of the mini- batch and then scaling and shifting the normalized output using learnable parameters γ and β [24]. The normalized output $\hat{x}$ is computed as in Eq. (6).

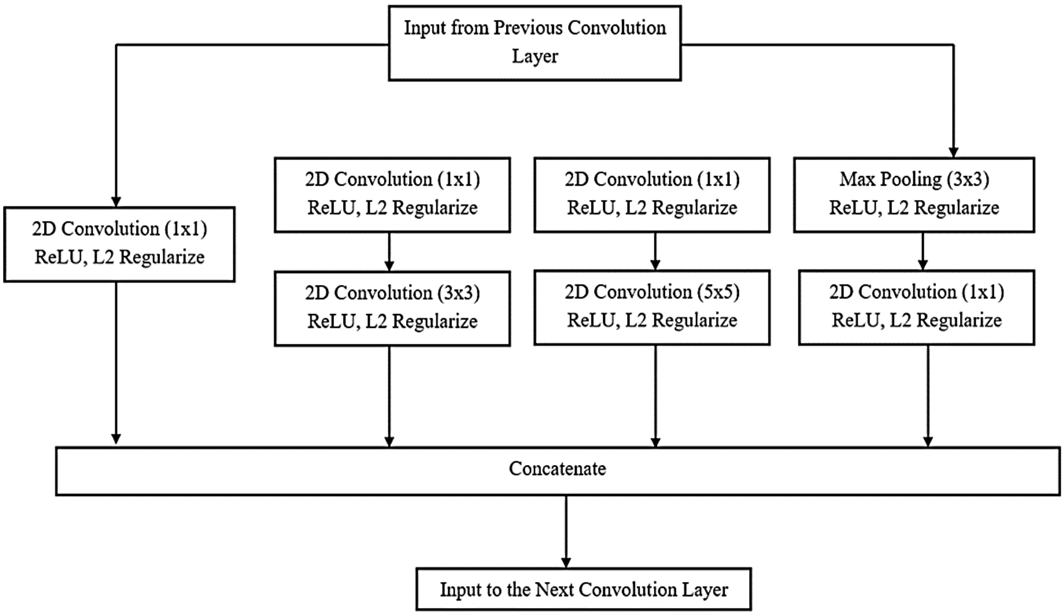

Figure. 18 Block Diagram of Inception Block

$$\hat{x} = \frac{x-\mu}{\sqrt{\sigma^2+\epsilon}} \tag{6}$$

Where ϵ is a minor constant introduced for numerical stability.

This normalized output is then scaled and shifted, expressed in Eq. (7).

$$y = \gamma\hat{x} + \beta \tag{7}$$

Batch normalization in the proposed model helps in reducing internal covariate shift, which allows for higher learning rates and faster convergence. It serves as a kind of regularization, reducing the dependence on dropout layers and enhancing the model's generalization to new data. L2 regularization is a method employed to mitigate overfitting in neural networks by incorporating a penalty into the loss function that is dependent upon the squared magnitude of the model's weights [25]. This regularization method inhibits complex models that might overfit the training set by keeping the weights minimal. In the proposed model, L2 regularization is applied to the convolutional and dense layers by adding the term $\lambda \sum_i w_i^2$ to the loss function, where w_i are the weights and λ is the regularization parameter. This can be mathematically expressed as in Eq. (8).

$$L_{total} = L_{Original} + \lambda \sum_i w_i^2 \tag{8}$$

By adjusting large weights, L2 regularization helps the model to achieve a compromise between fitting the training data and preserving simpler weight values. This regularization method complements other techniques like dropout and batch normalization, further boosting the model's capability to generalize well to new data. In the proposed approach, L2 regularization helps to improve robustness and performance by preventing the network from relying too heavily on any single feature.

The final layer of the proposed approach is a FC layer. In general, a FC layer is a feed-forward neural network. The final pooling or convolution layer's output layer sends flattened data as input to a FC layer. Pooling or a convolutional layer forms the output, then flattening separates and converts all values into vectors. Adding a FC layer with a sigmoid activation function creates a binary classification result that shows whether a brain tumor is present or not. The detailed algorithm of the suggested brain tumor detection model is explained below.

Algorithm: Brain Tumor Detection Model Using Hybrid Inception- CNN model with Hyperparameter Tuning from Microwave Brain Images

Input: *Microwave Brain Images*
Output: *Efficient Brain Tumor Detection Model*

Begin:

Load and preprocess data:

- *Collect dataset: D= {(X_i, y_i), where X_i is the microwave brain images and $y_i \in$ {0,1} $y_i i \in$ {0,1} (1: Tumor, 0: Healthy).*
- *Preprocess:*

Received: October 28, 2024. Revised: December 18, 2024.

- *Normalize:* $X_i' \rightarrow \frac{X_i' - \mu}{\sigma}$
- *Cropping*
- *Augmentation:* $X_i' \rightarrow \{X_i''\}$ *(Rotation, Shift, Shear, Flip)*

Define Inception Module:
branch1 = Conv2D () (x)
branch3 = Conv2D () (x)
branch3 = Conv2D () (branch3)
branch5 = Conv2D () (x)
branch5 = Conv2D () (branch5)
branch_pool = MaxPooling2D () (x)
branch_pool = Conv2D () (branch_pool)
x = concatenate ([branch1, branch3, branch5, branch_pool]
Define Hybrid Inception- CNN Module:
inputs = Input ()
x = Conv2D () (inputs)
x = BatchNormalization () (x)
x = MaxPooling2D () (x)
x = Dropout () (x)
x = Inception_model (x, 32)
x = MaxPooling2D () (x)
x = Dropout () (x)
x = Conv2D () (x)
x = MaxPooling2D () (x)
x = Dropout () (x)
x = Conv2D () (x)
x = MaxPooling2D () (x)
x = Dropout () (x)
x = Flatten () (x)
x = Dense () (x)
x = Dropout () (x)
outputs = Dense (1, activation='sigmoid') (x)
model = Model (inputs, outputs)
Model Compilation and Training:
- *Compile each model M:*
  optimizer=Adam (learning_rate)
  loss=binary_crossentropy
  metrics=[accuracy]
- *Train: M.fit (* X_{train} *,* y_{train} *,validation_data= (*X_{val}, y_{val}*))*

Model Evaluation and Comparison:
- *Evaluate:*
  metrics=M.evaluate(X_{test} *,* y_{test}*)*
- *Adjust Hyperparameters*

Save the Model:
End

3.2.4. Simulation setup and hyperparameter tuning

The Google Collaboratory platform has been utilized to train and evaluate the proposed framework using Python. Adam serves as the optimization algorithm for training, while binary crossentropy functions as the loss metric. The loss function quantifies the disparity between the true ground truth labels and the anticipated outputs produced by the network. It quantifies the alteration between the anticipated probability and the actual binary labels (0 or 1) for each data point. The training takes place over 20 epochs, with each epoch comprising iterations over batches of 32 samples at the same time. Table 2 tabulates various hyperparameters used in the proposed study.

Table. 2 Hyperparameters

Hyperparameters	Values
Batch Size	32
Activation Function	Sigmoid
Optimizer	Adam
Dropout Rate	0.5, 0.6, 0.7, 0.8
Number of Epochs	20
Learning Rate	0.0001
Loss Function	Binary Cross Entropy

CNN modifies several hyperparameters that influence the model's efficacy, including the number of epochs, selected batch size, activation function, learning rate and dropout rate. The hyperparameter tuning method involves repeated experiments with different quantities of hidden layers, epochs, activation functions, and learning rates. Adjusting these parameters enhances the accuracy of CNN models.

4. Results and discussion

4.1 Performance evaluation of suggested UWB circular monopole patch antenna

Transmission line discontinuities always reflect or return a portion of the signal power to the source when it travels over a transmission line. The connector, transmission line, or system connection could be the source of the discontinuity. This reflected power measurement is known as RL. The RL is mathematically expressed as in Eq. (9).

$$RL = 10 \log_{10} \frac{P_i}{P_r} \tag{9}$$

The measured and simulated RL of the fabricated antenna is visualized in Fig. 19. The fabricated antenna shows a RL of -20.24 dB at 4.6 GHz, -48.3 dB at 7.68 GHz, and -26.3 dB at 10.46 GHz. It was able to reach 4.6GHz-10.6GHz UWB BW. The changes in measured RL are due to errors in SMA connector in the feed line.

Fig. 20 illustrates the variation in RL with respect to DGS. The DGS has a partial ground plane with two inverted U-slots that make the circular monopole antenna with a microstrip feed work with a wider range of frequencies. This design modification reduces the surface current distribution on the patch antenna due to the presence of the DGS at the current plane. The integration of DGS enhances impedance matching, leading to improved RL. The DGS enhances the antenna's overall performance by modifying the existing routes and redistributing the surface currents.

As a result, the circular monopole antenna's operating BW increases and becomes more efficient. The antenna with DGS exhibited superior reflection coefficients of 24.56 dB at 4.7 GHz, 31.98 dB at 7.7 GHz, and -21.8 dB at 10.5 GHz. Fig. 21 visualizes the variation in RL with respect to square slot. The design of a slotted antenna underwent an experimental study that showed significant effects on RL, BW, and impedance matching. The suggested design incorporates a circular monopole antenna with a central square slot in the patch. The square slot modified the current distribution on the patch antenna, resulting in enhanced RL, signifying higher signal efficiency. The improved design improves impedance matching, ensuring excellent performance across a wider frequency range. The circular monopole antenna has a superior RL of 48.5 dB with a square slot and 41.2 dB without a square slot.

Fig. 22 illustrates the variation in RL with respect to the length of ground plane. The ground length has been tuned by shifting between L_g = 23.5 mm and L_g = 25.5 mm, with a step size of 1 mm, to get UWB impedance matching properties for MI in brain tumor detection. This optimization technique ensures the antenna functions effectively across an extensive frequency range, essential for precise imaging. Optimizing the ground length improves impedance matching, resulting in better signal transmission and reception. In MI applications, the optimized ground length enhances detection capability. Enhancing this ground length results in improved impedance matching at the frequency of 7.68 GHz at -48.3 dB for L_g= 24.5 mm. Fig. 23 illustrates the variation of RL with respect to radius of circular patch. Optimizing the patch radius results in improved impedance matching and a high gain of -41.3dB at a frequency of 7.68GHz for a radius of 11mm. This finding demonstrated that reaching impedance matching depends on the patch variation's radius. Fig. 24 illustrates the variation of RL with respect to feed length. By improving the patch's feed length, the frequency of 7.68 GHz at -41.3 dB for L_f = 37 mm yields better impedance matching and high gain.

The voltage standing wave ratio (VSWR) measures the radio frequency power transmission efficiency from a power source over a transmission line. VSWR is mathematically expressed as in Eq. (10), where Γ is the reflection coefficient.

$$VSWR = \frac{1+|\Gamma|}{1-|\Gamma|} \tag{10}$$

The measured and simulated VSWR of the fabricated antenna is shown in Fig. 25. Both curves exhibit similar patterns, with a VSWR that remains below 2.0 for the majority of the frequency spectrum, indicating excellent impedance matching. Overall, the alignment of the two results demonstrates the antenna design's correctness and dependability. But there are a few minor variations between the measured and simulated data, particularly in the area of the resonance peaks.

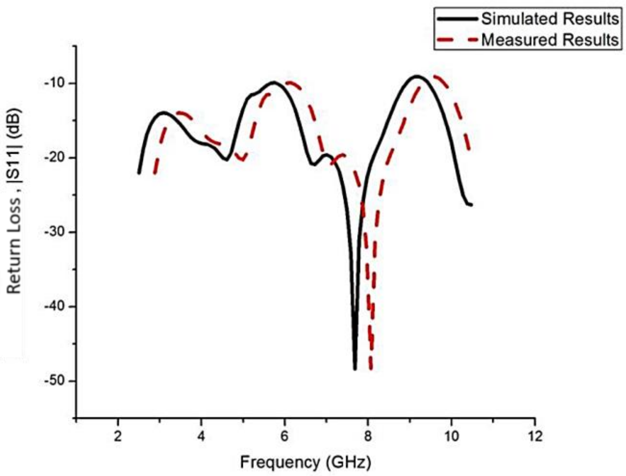

Figure. 19 Simulated and Measured RL of Fabricated Antenna

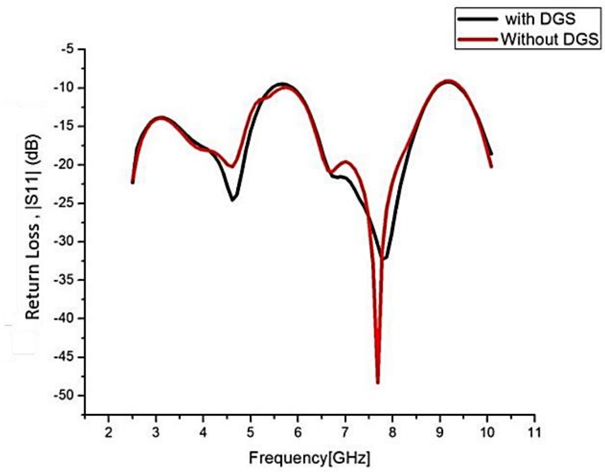

Figure. 20 Variation of RL with respect to DGS

Received: October 28, 2024. Revised: December 18, 2024.

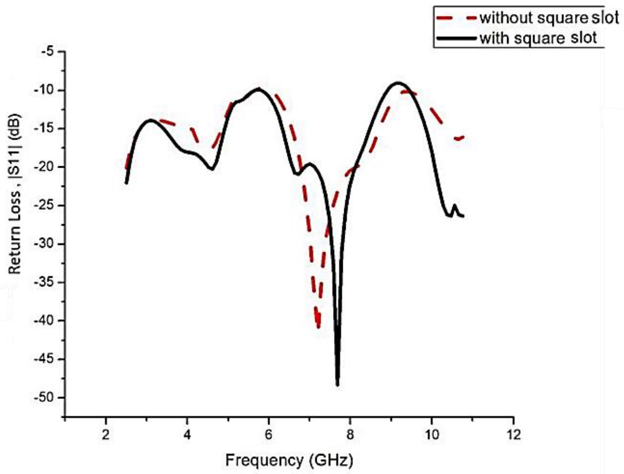

Figure. 21 Variation of RL with respect to Square Slot

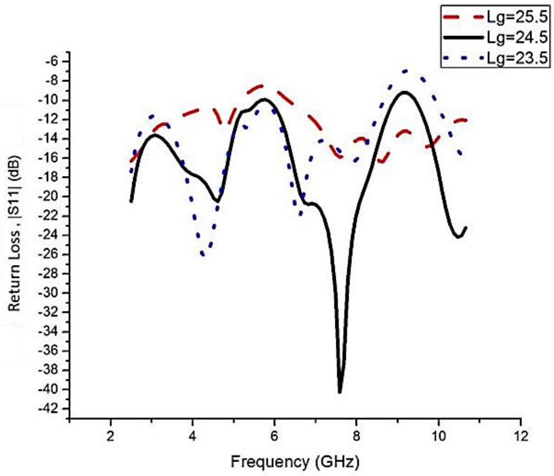

Figure. 22 Variation of RL with respect to Length of Ground Plane

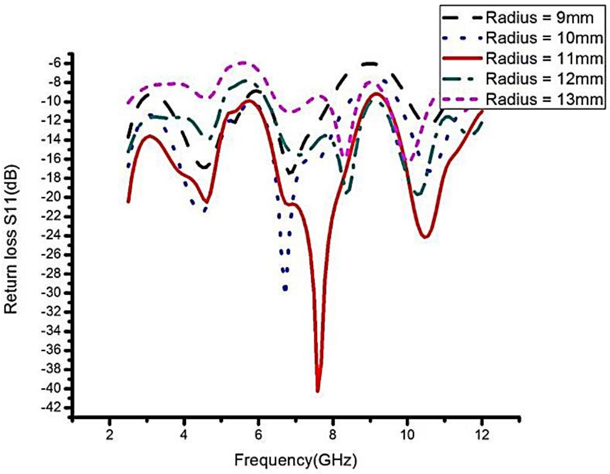

Figure. 23 Variation of RL with respect to Radius of Circular Patch

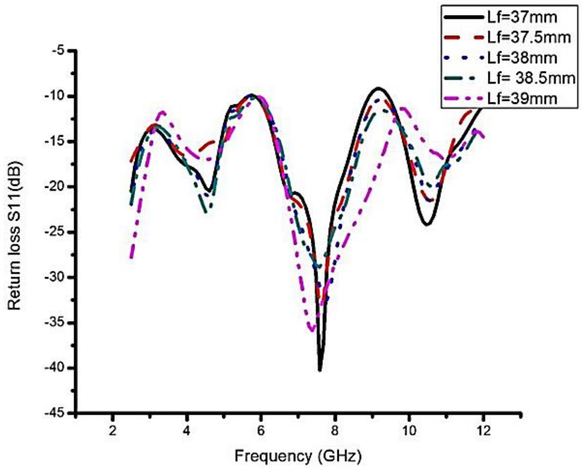

Figure. 24 Variation of RL with respect to Feed Length

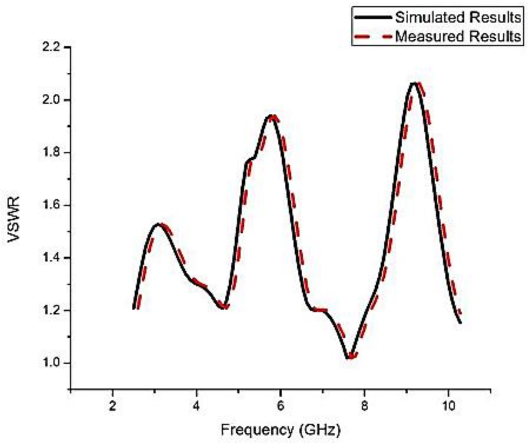

Figure. 25 Simulated and Measured VSWR of Fabricated Antenna

Fig. 26 illustrates the current distribution of the fabricated antenna. The circular disc monopole antenna's middle section has a lower current density; therefore, cutting it out doesn't have a big impact on the current flow overall. The longer effective route of the surface current ensures stable performance.

Received: October 28, 2024. Revised: December 18, 2024.

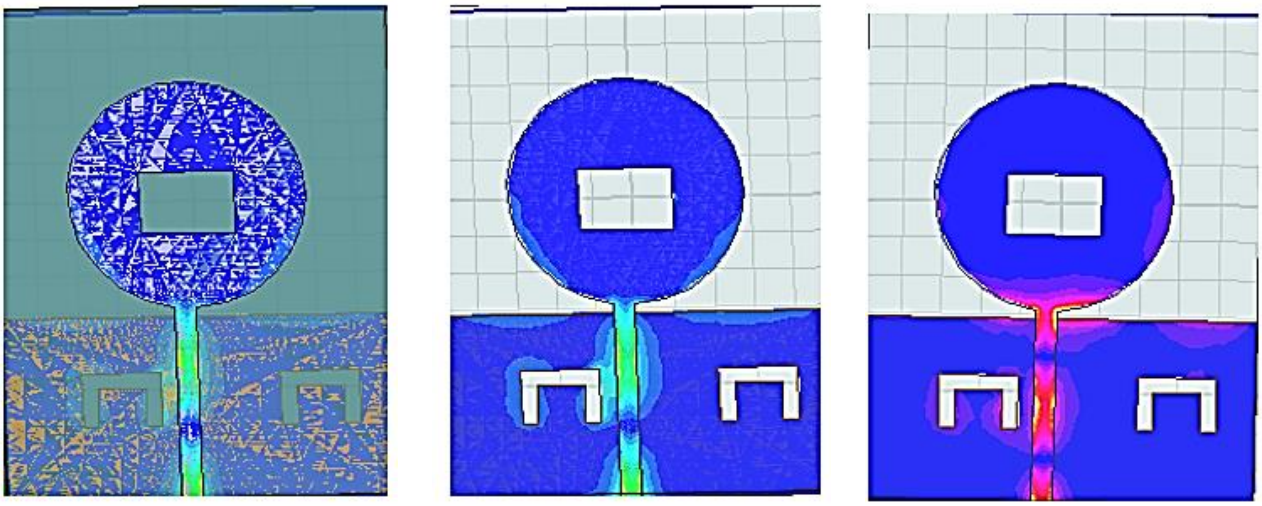

(a) (b) (c)

Figure. 26 Current Distribution of the Fabricated Antenna: (a)4.6 GHz, (b)7.7 GHz, and (c)10 GHz

This antenna design enhances BW by etching a square slot in the middle of the monopole antenna. This deliberate adjustment increases BW without disrupting the existing distribution, therefore preserving the antenna's efficiency and performance. At 4.6 GHz, the current is primarily localized around the circular patch and the feedline, indicating robust resonance at this frequency. As the frequency rises to 7.7 GHz, the current distribution broadens and intensifies, encompassing a greater expanse of the circular patch and the feedline. At 10 GHz, the current intensity peaks, especially around the feedline and the outer edges of the circular patch, indicating substantial energy radiation at this frequency. The changes in current distribution at various frequencies underscore the antenna's capability to function efficiently throughout an extensive frequency range.

The E- plane and H- plane radiation pattern of fabricated antenna is shown in Figs. 27 and 28 respectively. The E-plane's radiation pattern resembles a butterfly, exhibiting strong nulls at specific angles. This means that there is strong directivity in two opposite directions. Similar to the E-plane, the H-plane pattern exhibits directivity, but it is a little more omnidirectional.

The gain plot and directivity plot of antenna is shown in Figs. 29 and 30 respectively. Within the UWB frequency range of 3-10 GHz, the proposed circular monopole patch antenna's simulated design achieved a gain of around 5.32 dBi and a directivity of 6.52 dB.

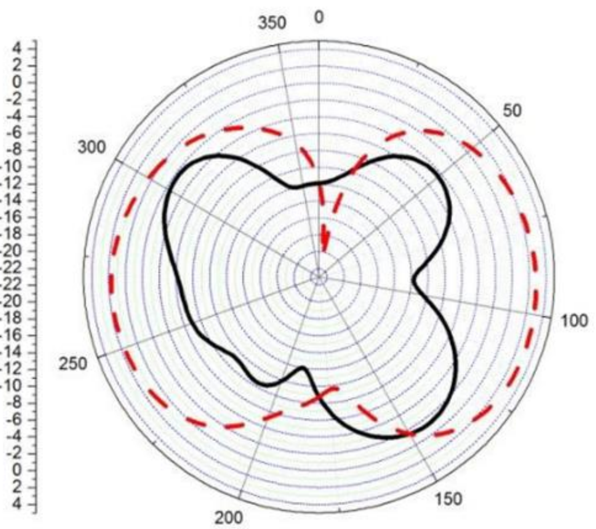

Figure. 27 E-plane Radiation Pattern at 7.7GHz

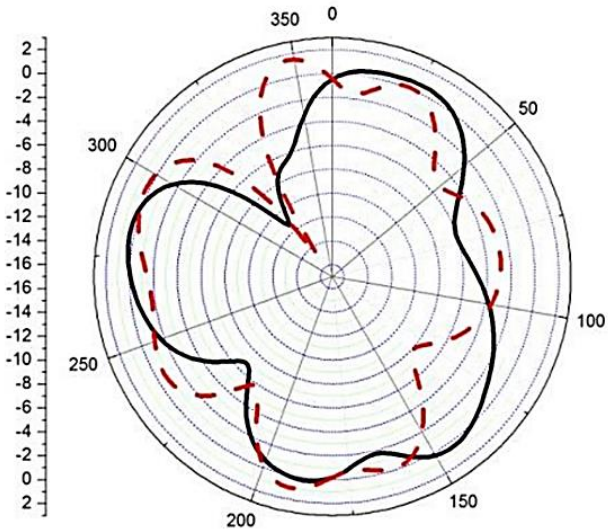

Figure. 28 H-plane Radiation Pattern at 7.7 GHz

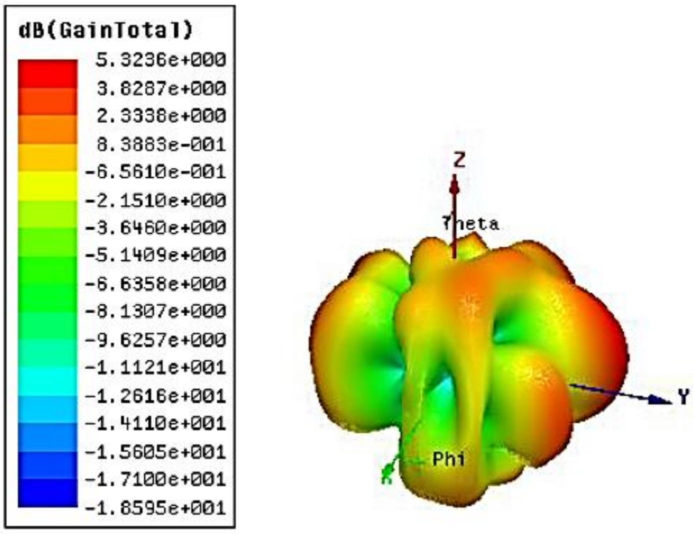

Figure. 29 Gain Plot

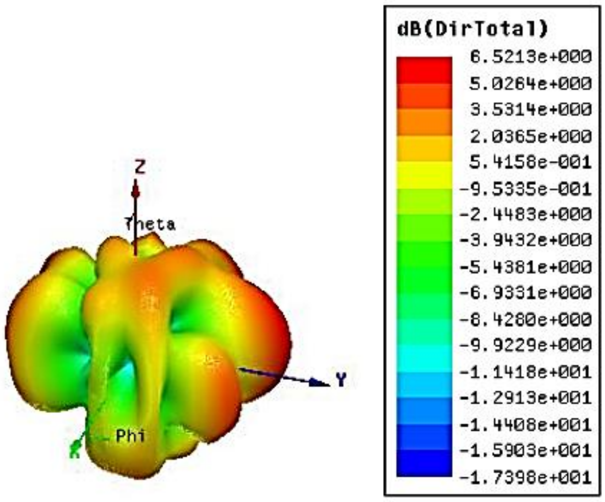

Figure. 30 Directivity Plot

4.2 Performance evaluation of proposed brain tumor detection model

Figs. 31 and 32 respectively illustrates the accuracy and loss plots of the suggested brain tumor detection model. The proposed model undergoes training for 20 epochs. The model initially exhibits a substantial improvement, with accuracy increasing from 54.10 % to 95.85 % and training loss decreasing from 12.4 to 5.4. The validation accuracy begins from 74.57% to 99.42 %.

Table 3 presents the evaluation measures that have been employed to assess the performance of the suggested brain tumor detection approach. Table 4 tabulates the classification report of the suggested brain tumor detection model. The model accurately classifies brain tumor cases, with a 99.48% accuracy rate. The model accurately detects all positive and negative cases, with no false positives or false negatives, as evidenced by the recall and specificity both reaching 1.0000.

The model ensures both high sensitivity and precision by maintaining a strong balance between recall and precision, as seen by the precision of 0.9900 and the high F1-score of 0.9950. The Cohen's Kappa score of 0.9896 indicates the near-perfect agreement between the true and predicted classifications, supporting the model's reliability. The ROC AUC value of 0.9950 indicates the model's exceptional capability to distinguish between classes. The classification report of individual classes is illustrated in Fig. 33.

Fig. 34 displays the confusion matrix of the suggested brain tumor detection system.

Received: October 28, 2024. Revised: December 18, 2024.

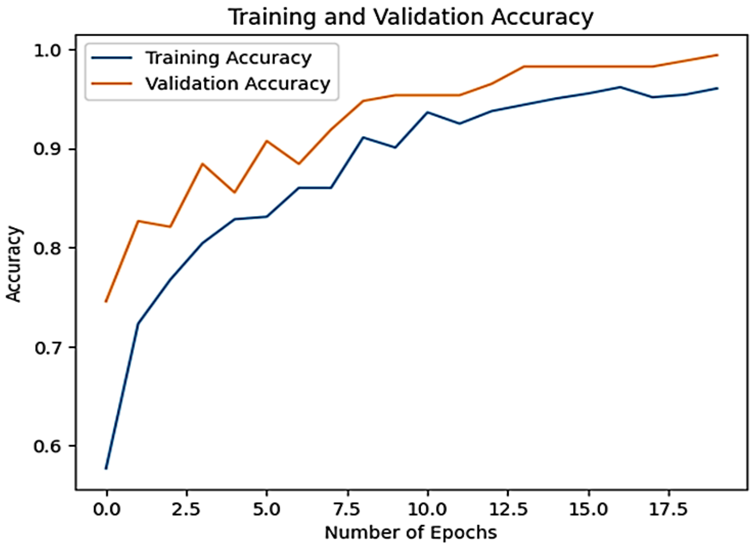

Figure. 31 Accuracy Plot of Proposed Brain Tumor Detection Model

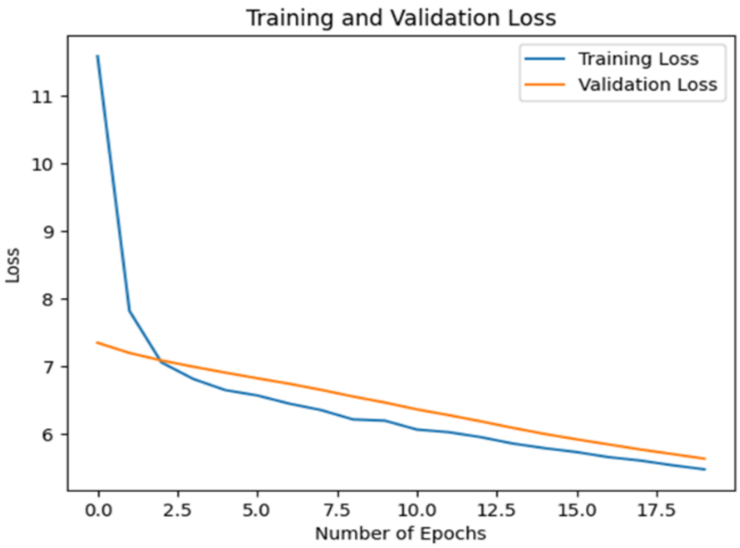

Figure. 32 Loss Plot of Proposed Brain Tumor Detection Model

Table 3. Evaluation Metrics Utilized for Brain Tumor Detection System

Performance Parameters	Equation
Accuracy	$\frac{(True\ Positive + True\ Negative)}{(True\ Positive + True\ Negative + False\ Positive + False\ Negative)}$
Precision	$\frac{(True\ Positive)}{(True\ Positive + Fasle\ Positive)}$
Recall	$\frac{(True\ Positive)}{(True\ Positive + False\ Negative)}$
F1- Score	$2 \times (\frac{Precision \times Recall}{Precision + Recall})$
Specificity	$\frac{(True\ Negative)}{(True\ Negative + False\ Positive)}$

Received: October 28, 2024. Revised: December 18, 2024.

Table. 4 Classification Report of Proposed Brain Tumor Detection Model

Performance Metrics	Obtained Results
Accuracy	0.9948
Recall	1.0000
Precision	0.9900
F1- Score	0.9950
Cohens Kappa	0.9896
ROC AUC	0.9950
Specificity	1.0000

	precision	recall	f1-score	support
0.0	0.99	1.00	0.99	92
1.0	1.00	0.99	1.00	101
accuracy			0.99	193
macro avg	0.99	1.00	0.99	193
weighted avg	0.99	0.99	0.99	193

Figure. 33 Classification Report of Individual Classes

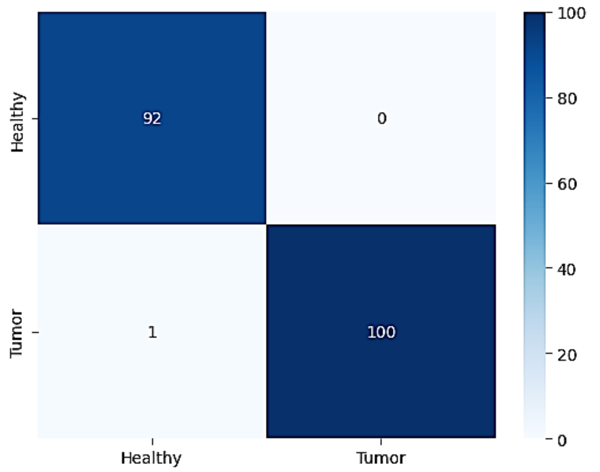

Figure. 34 Confusion Matrix of Proposed Brain Tumor Detection Model

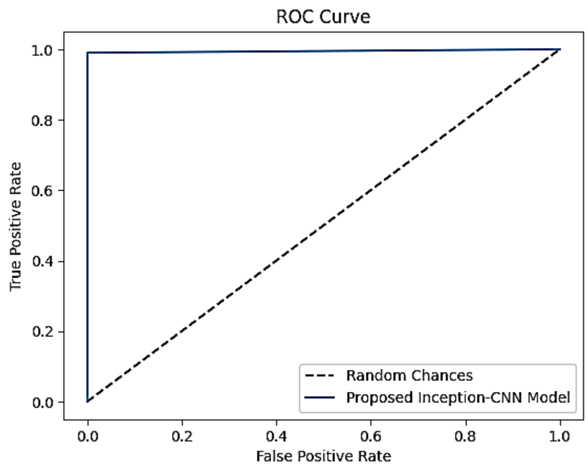

Figure. 35 ROC Curve of the Suggested Brain Tumor Detection Model

The suggested approach successfully classified all 92 of the true negative cases as negative, meaning there were no false positives among the 92 cases. Furthermore, out of 101 positive cases, the model accurately recognized 100 as positive, resulting in a single false negative. This yields a high true negative rate (specificity) and a high true positive rate (recall), underscoring the model's exceptional ability to successfully discriminate between the presence and absence of a brain tumor.

Fig. 35 illustrates the ROC curve produced by the suggested methodology, offering a visual depiction of the variations in true positive rate and true negative rate across different decision thresholds.

Fig. 36 illustrates the random samples of 10 test images, along with their predicted and ground truth labels. The title exhibits the predicted label alongside the true label, with the text colour displayed in green when the prediction is accurate.

Table 5 tabulates the performance comparison of the existing brain tumor detection system with the suggested model. The hybrid Inception-CNN model used in the suggested brain tumor detection system performs better than current techniques. With 99.48% accuracy, 99% precision, 100% recall, 99.50% F1-score, and 100% specificity, it surpasses methods such as MBINet, which achieved 96.97% accuracy and 96.93% precision, and the fine-tuned ResNet101 model, which obtained 95.90% accuracy. It also exceeds the fine-tuned EfficientNet, which achieved 98.8% accuracy and 99.4% precision, as well as the multiclass SVM method with an accuracy of 98.92%. While the Deep Neural Network Correlation Learning obtained excellent specificity (99.62%), its accuracy (97.5%) is considerably lower than the proposed method. Furthermore, techniques such as YOLO v5 and CNN consistently underperform across all critical measures, highlighting the exceptional robustness and efficiency of the proposed system.

The visualization of the performance comparison is displayed in Fig. 37. The high accuracy of EfficientNet is a result of its scalability in balancing depth, width, and resolution. However, because of its wide range of parameters, the model might need a lot of processing power. It lacks interpretability in decision-making processes and is susceptible to overfitting if not properly adjusted. SVM is very good at classifying data into binary or multiclass categories, but it is not very good at handling big datasets or learning hierarchical features from data. SVM frequently requires manual feature engineering because it is unable to automatically extract features, in contrast to neural networks. MBINet is a lightweight, task-specific network that works well

Received: October 28, 2024. Revised: December 18, 2024.

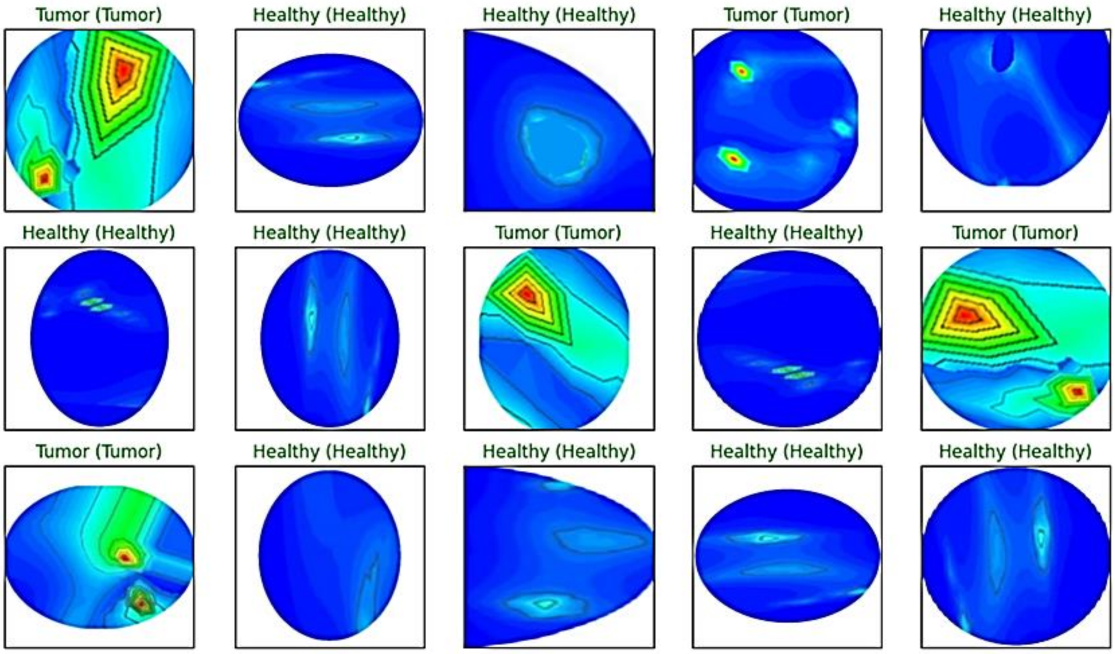

Figure. 36 Detection Outputs of Random Images

Table. 5 Performance Comparison

Authors & Year	**Methodology**	**Accuracy (%)**	**Precision (%)**	**Recall (%)**	**F1- Score (%)**	**Specificity (%)**
Amran Hossain *et al.* [26], (2023)	MBINet	96.97	96.93	96.85	96.83	97.95
Usman Zahid *et al.* [27], (2022)	Fine-tuned ResNet101	95.90	95.96	95.89	95.86	95.89
Hasnain Ali Shah *et al.* [28], (2022)	Fine-tuned EfficientNet	98.8	99.4	99.5	98.9	99.2
Sarmad Maqsood *et al.* [29], (2022)	Multiclass Support Vector Machine	98.92	-	98.82	-	99.02
Marcin Woz´niak *et al.* [30], (2023)	Deep Neural Network Correlation Learning	97.5	97.69	97.47	-	99.62
Amran Hossain *et al.* [31], (2022)	YOLO v5	96.32	95.17	94.98	95.53	95.28
Suraj Patil and Dnyaneshwar Kirange [32], (2023)	Ensemble DCNN	97.77	96.66	98.30	97.47	98.33
Mohamed Amine Mahjoubi *et al.* [33], (2023)	CNN	95.44	-	95	95.36	-
Proposed (Hybrid Inception-CNN)		**99.48**	**99**	**100**	**99.50**	**100**

Received: October 28, 2024. Revised: December 18, 2024.

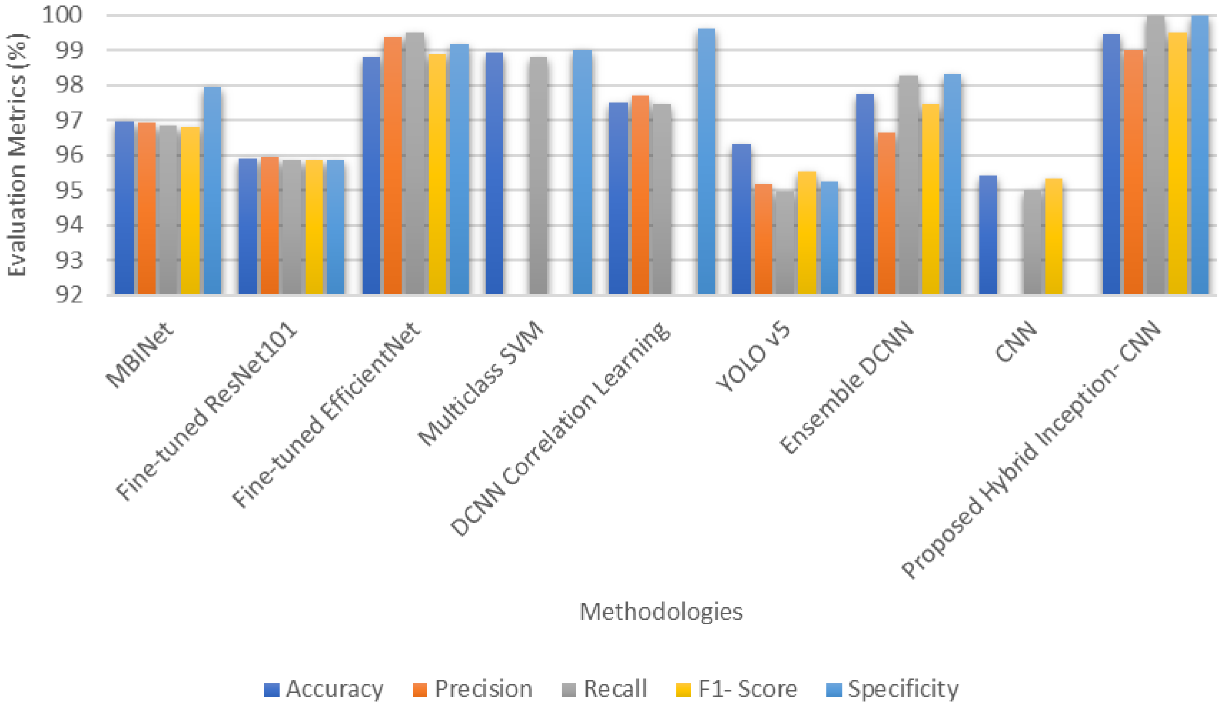

Figure. 37 Graphical Visualization of Performance Comparison in terms of Detection Accuracy

but might not be generalizable to a variety of datasets. It may sacrifice feature extraction accuracy and depth in favour of faster processing times. Residual connections help ResNet101 overcome vanishing gradient problems. Its deep architecture, however, may result in overfitting and higher processing expenses. Although it works well for feature extraction, it might not be the best option for datasets that need highly localized or multi-scale feature analysis. By combining predictions from several models, the ensemble approach improves generalization. The rise in training complexity and computational overhead, however, may be a disadvantage. Ensemble models are less appropriate for real-time applications due to their high resource requirements. The goal of YOLO v5 is to detect objects quickly and accurately. Although efficient, it might have trouble with tasks that call for exact boundary delineation. It is not ideal for situations where fine-grained feature extraction is prioritized due to its emphasis on speed over accuracy. The model's ability to recognize relationships in the data is enhanced by correlation learning. However, optimizing hyperparameters is necessary to achieve high performance. When dealing with noisy or unbalanced datasets, it might not be as robust. The best approach is the hybrid Inception-CNN because of its exceptional ability to balance F1-score, recall, specificity, accuracy, and precision. The strength of its architecture is its capacity to effectively handle multi-scale features while avoiding the problems of overfitting or excessive computational demands.

5. Conclusion

The proliferation of aberrant cells in brain tissue can become uncontrolled and lead to brain tumors. A benign brain tumor does not adversely affect surrounding healthy tissue, whereas a malignant tumor can inflict damage and could result in cerebral haemorrhage. Timely identification of brain tumors is critical for ensuring patient survival. In this paper, an effective DL-based method for microwave brain image-based brain tumor detection was proposed. It mostly consisted of two phases. Initially, an UWB circular monopole patch antenna and a head phantom model are developed for MI. In the second phase, a hybrid inception-CNN model for AI-based detection was implemented. The images obtained from the patch antenna system are fed into the hybrid inception-CNN to extract high-level features. The FC layer processed the collected features for effective brain tumor categorization. The simulation results exhibited outstanding performance, achieving an accuracy of 99.48%, precision of 100%, recall of 99.00%, F1-score of 99.50%, and specificity of 100%. This method uses brain tissue's electromagnetic properties and AI power to provide an alternative way to diagnose brain tumors in real time without surgery.

Conflicts of Interest

The authors declare that there are no conflicts of interest related to this manuscript.

Author Contributions

The authors confirm contribution to the paper as follows: study conception and design: Deebu U S, Sreeja T K; data collection: Deebu U S; analysis and interpretation of results: Deebu U S, Sreeja T K; draft manuscript preparation: Deebu U S. All authors reviewed the results and approved the final version of the manuscript.

Acknowledgments

I would like to express my sincere gratitude to all those who contributed to the completion of this research paper. I extend my heartfelt thanks to my supervisor, my family, my colleagues and fellow researchers for their encouragement and understanding during the demanding phases of this work.

References

[1] K. J. Zülch, *Brain Tumors: Their Biology and Pathology*, Springer Science & Business Media, 2012.

[2] M. Pastorino, *Microwave Imaging*, Wiley Publication, 2010.

[3] H. G. Schantz, "Introduction to ultra-wideband antennas", In: *Proc. of IEEE Conference on Ultra-Wideband Systems and Technologies*, pp. 1-9, 2003.

[4] K. Gopalakrishnan, A. Adhikari, N. Pallipamu, M. Singh, T. Nusrat, S. Gaddam, et al., "Applications of microwaves in medicine leveraging artificial intelligence: Future perspectives", *Electronics*, Vol. 12, No. 5, p. 1101, 2023.

[5] A. G. Derneryd, "Linearly polarized microstrip antennas", *IEEE Trans. Antennas Propag.*, pp. 846-851, 1976.

[6] Y. T. Lo, D. Solomon, and W. F. Richards, "Theory and experiment on microstrip antennas", *IEEE Trans. Antennas Propag.*, Vol. AP-27, No. 2, pp. 137-145, 1979.

[7] P. C. Jackson, *Introduction to Artificial Intelligence*, Courier Dover Publications, 2019.

[8] N. Goswami and M. A. Rahman, "Design of a UWB patch antenna and performance evaluation in detecting brain tumors", *e-Prime - Advances in Electrical Engineering, Electronics and Energy*, Vol. 100623, 2024.

[9] M. Samsuzzaman, M. S. Talukder, A. Alqahtani, A. G. Alharbi, R. Azim, M. S. Soliman, and M. T. Islam, "Circular slotted patch with defected grounded monopole patch antenna for microwave-based head imaging applications", *Alexandria Engineering Journal*, Vol. 65, pp. 41-57, 2023.

[10] M. N. Hamza, M. T. Islam, and S. Koziel, "Advanced sensor for non-invasive breast cancer and brain cancer diagnosis using antenna array with metamaterial-based AMC", *Engineering Science and Technology, an International Journal*, Vol. 56, p. 101779, 2024.

[11] H. V. Kumar and T. S. Nagaveni, "Design of microstrip patch antenna to detect breast cancer", *ICTACT Journal on Microelectronics*, Vol. 6, No. 1, pp. 893-896, 2020.

[12] I. Jahan and A. Kabir, "Microstrip patch antenna for breast cancer detection", In: *Proc. of 2021 5th International Conference on Electrical Information and Communication Technology (EICT)*, pp. 1-6, 2021.

[13] R. Singh, N. Narang, D. Singh, and M. Gupta, "Compact wideband microstrip patch antenna design for breast cancer detection", *Defence Science Journal*, Vol. 71, No. 3, 2021.

[14] D. Kumar and D. Mathur, "A soft surface-based low-profile wearable antenna for biomedical telemetry", *International Journal of Electrical and Electronic Engineering & Telecommunications*, Vol. 11, No. 5, pp. 356–362, 2022.

[15] S. Alhuwaidi and T. Rashid, "A novel compact wearable microstrip patch antenna for medical applications", In: *Proc. of 2020 International Conference on Communications, Signal Processing, and Their Applications (ICCSPA)*, pp. 1-6, 2021.

[16] A. Wajid, A. Ahmad, S. Ullah, D. Y. Choi, and F. U. Islam, "Performance analysis of wearable dual-band patch antenna based on EBG and SRR surfaces", *Sensors*, Vol. 22, No. 14, p. 5208, 2022.

[17] P. Laxman and A. Jain, "A novel wearable free-wideband antenna circularly polarized suited for biotelemetric devices with multiple-input multiple-output and high data rate capacity", *The Journal of Engineering*, Vol. 2022, No. 6, pp. 595-607, 2022.

[18] M. E. Yassin, K. F. Hussein, Q. H. Abbasi, M. A. Imran, and S. A. Mohassieb, "Flexible antenna with circular/linear polarization for wideband biomedical wireless communication", *Sensors*, Vol. 23, No. 12, p. 5608, 2023.

[19] M. S. U. Rahman, O. S. Hassan, A. A. Mustapha, M. A. Abou-Khousa, and W. J. Cantwell, "Microwave NDT of smart composite structures with embedded antennas", *Sensors*, Vol. 23, No. 6, p. 3200, 2023.

[20] K. O'Shea, "An introduction to convolutional neural networks", *arXiv preprint arXiv:1511.08458*, 2015.

[21] Y. Pang, M. Sun, X. Jiang, and X. Li, "Convolution in convolution for network in network", *IEEE Transactions on Neural Networks and Learning Systems*, Vol. 29, No. 5, pp. 1587-1597, 2017.

[22] A. Zafar, M. Aamir, N. Mohd Nawi, A. Arshad, S. Riaz, A. Alruban, ... and S. Almotairi, "A comparison of pooling methods for convolutional neural networks", *Applied Sciences*, Vol. 12, No. 17, p. 8643, 2022.

[23] C. Banerjee, T. Mukherjee, and E. Pasiliao, "An empirical study on generalizations of the ReLU activation function", In: *Proc. of the 2019 ACM Southeast Conference*, pp. 164-167, 2019.

[24] N. Bjorck, C. P. Gomes, B. Selman, and K. Q. Weinberger, "Understanding batch normalization", *Advances in Neural Information Processing Systems*, Vol. 31, 2018.

[25] C. Cortes, M. Mohri, and A. Rostamizadeh, "L2 regularization for learning kernels", *arXiv preprint arXiv:1205.2653*, 2012.

[26] C. N. Ladefoged, L. Marner, A. Hindsholm, I. Law, L. Højgaard, and F. L. Andersen, "A lightweight deep learning-based microwave brain image network model for brain tumor classification using reconstructed microwave brain (RMB) images", *Biosensors*, Vol. 13, No. 2, p. 238, 2023.

[27] Chato, L., & Latifi, S., "BrainNet: optimal deep learning feature fusion for brain tumor classification", *Computational Intelligence and Neuroscience*, Vol. 2022, p. 2022.

[28] Y. Bhanothu, A. Kamalakannan, and G. Rajamanickam, "A robust approach for brain tumor detection in magnetic resonance images using finetuned efficientnet", *IEEE Access*, Vol. 10, pp. 65426-65438, 2022.

[29] S. Maqsood, R. Damaševičius, and R. Maskeliūnas, "Multi-modal brain tumor detection using deep neural network and multiclass SVM", *Medicina*, Vol. 58, No. 8, p. 1090, 2022.

[30] M. Woźniak, J. Siłka, and M. Wieczorek, "Deep neural network correlation learning mechanism for CT brain tumor detection", *Neural Computing and Applications*, Vol. 35, No. 20, pp. 14611-14626, 2023.

[31] A. Hossain, M. T. Islam, and A. F. Almutairi, "A deep learning model to classify and detect brain abnormalities in portable microwave-based imaging system", *Scientific Reports*, Vol. 12, No. 1, p. 6319, 2022.

[32] S. Patil and D. Kirange, "Ensemble of deep learning models for brain tumor detection", *Procedia Computer Science*, Vol. 218, pp. 2468-2479, 2023.

[33] M. A. Mahjoubi, S. Hamida, O. E. Gannour, B. Cherradi, A. E. Abbassi, and A. Raihani, "Improved multiclass brain tumor detection using convolutional neural networks and magnetic resonance imaging", *Int. J. Adv. Comput. Sci. Appl.*, Vol. 14, No. 3, 2023.